



AFRL-OSR-VA-TR-2013-0519

**SCATTERING TOOLS FOR NANOSTRUCTURE PHONON
ENGINEERING**

PAUL EVANS

UNIVERSITY OF WISCONSIN SYSTEM

**09/25/2013
Final Report**

DISTRIBUTION A: Distribution approved for public release.

**AIR FORCE RESEARCH LABORATORY
AF OFFICE OF SCIENTIFIC RESEARCH (AFOSR)/RSA
ARLINGTON, VIRGINIA 22203
AIR FORCE MATERIEL COMMAND**

REPORT DOCUMENTATION PAGE				Form Approved OMB No. 0704-0188	
<p>The public reporting burden for this collection of information is estimated to average 1 hour per response, including the time for reviewing instructions, searching existing data sources, gathering and maintaining the data needed, and completing and reviewing the collection of information. Send comments regarding this burden estimate or any other aspect of this collection of information, including suggestions for reducing the burden, to the Department of Defense, Executive Service Directorate (0704-0188). Respondents should be aware that notwithstanding any other provision of law, no person shall be subject to any penalty for failing to comply with a collection of information if it does not display a currently valid OMB control number.</p> <p>PLEASE DO NOT RETURN YOUR FORM TO THE ABOVE ORGANIZATION.</p>					
1. REPORT DATE (DD-MM-YYYY) 09-21-2013		2. REPORT TYPE Final Report		3. DATES COVERED (From - To) 06-15-2010 - 06-14-2013	
4. TITLE AND SUBTITLE Scattering Tools for Nanostructure Phonon Engineering				5a. CONTRACT NUMBER	
				5b. GRANT NUMBER AFOSR FA9550-10-1-0249	
				5c. PROGRAM ELEMENT NUMBER	
6. AUTHOR(S) Paul G. Evans Kyle M. McElhinny Gokul Gopalakarishnan				5d. PROJECT NUMBER	
				5e. TASK NUMBER	
				5f. WORK UNIT NUMBER	
7. PERFORMING ORGANIZATION NAME(S) AND ADDRESS(ES) Department of Materials Science and Engineering University of Wisconsin-Madison 1509 University Ave. Madison, WI 53706				8. PERFORMING ORGANIZATION REPORT NUMBER	
9. SPONSORING/MONITORING AGENCY NAME(S) AND ADDRESS(ES) Air Force Office of Science and Research 875 Randolph Street Suite 325 Room 3112 Arlington, VA 22203				10. SPONSOR/MONITOR'S ACRONYM(S) AFOSR	
				11. SPONSOR/MONITOR'S REPORT NUMBER(S)	
12. DISTRIBUTION/AVAILABILITY STATEMENT					
13. SUPPLEMENTARY NOTES					
14. ABSTRACT <p>The vibrational properties of solids have crucial roles underpinning functional properties ranging from thermal conductivity to electron mobility. It has long been known that the modification of the mechanical boundary conditions imposed by the minimal spatial extent of nanostructures results in changes in the phonon dispersion. These changes include the creation of vibrational modes with symmetries not permitted by the bulk crystal, but allowed in nanostructures. The new modes are predicted to have wavevectors with magnitudes that range across the entire Brillouin zone of reciprocal space. These new modes present a serious characterization challenge because existing experimental techniques for the characterization of phonons in nanomaterials, such as Raman scattering, are sensitive only to phonon modes with wavevectors of extremely small magnitude. Fundamentally the wavevectors that can be probed by Raman scattering are limited by the small momentum of photons in the visible spectrum. Our work supported by this grant from the AFOSR has addressed the phonon characterization problem using x-ray scattering. Our approach is based on an adapting x-ray thermal diffuse scattering (TDS) techniques to nanoscale systems. With this approach we can probe phonons across the</p>					
15. SUBJECT TERMS <p>nanomaterials, phonons, x-ray scattering, nanomembrane fabrication, flatness, large-wavevector vibrational properties, synchrotron x-rays, thermal diffuse scattering, silicon nanomembranes</p>					
16. SECURITY CLASSIFICATION OF:			17. LIMITATION OF ABSTRACT	18. NUMBER OF PAGES	19a. NAME OF RESPONSIBLE PERSON Paul Gregory Evans
a. REPORT	b. ABSTRACT	c. THIS PAGE			19b. TELEPHONE NUMBER (Include area code) (608) 265-6773

Scattering Tools for Nanostructure Phonon Engineering

Final Report for AFOSR FA9550-10-1-0249

September, 2013

Kyle M. McElhinny,¹ Gokul Gopalakrishnan,¹ and Paul G. Evans,^{1,a}

¹ Department of Materials Science and Engineering and Materials Science Program, University of Wisconsin, 1509 University Ave., Madison, WI 53706

^a Email: evans@engr.wisc.

Abstract

The vibrational properties of solids have crucial roles underpinning functional properties ranging from thermal conductivity to electron mobility. It has long been known that the modification of the mechanical boundary conditions imposed by the minimal spatial extent of nanostructures results in changes in the phonon dispersion. These changes include the creation of vibrational modes with symmetries not permitted by the bulk crystal, but allowed in nanostructures. The new modes are predicted to have wavevectors with magnitudes that range across the entire Brillouin zone of reciprocal space. These new modes present a serious characterization challenge because existing experimental techniques for the characterization of phonons in nanomaterials, such as Raman scattering, are sensitive only to phonon modes with wavevectors of extremely small magnitude. Fundamentally the wavevectors that can be probed by Raman scattering are limited by the small momentum of photons in the visible spectrum.

Our work supported by this grant from the AFOSR has addressed the phonon characterization problem using x-ray scattering. Our approach is based on an adapting x-ray thermal diffuse scattering (TDS) techniques to nanoscale systems. With this approach we can probe phonons across the full range of wavevectors, the entire Brillouin zone, from sample volumes as small as 4 cubic microns. We have demonstrated the TDS approach using silicon nanomembranes with a series of thicknesses as small as 4 nm. TDS techniques required membranes far flatter than what had been possible previous fabrication techniques and we have thus developed an edge-induced flattening technique that provides unprecedented flatness. The TDS experiments were conducted using synchrotron x-rays at the experimental facilities of the Advanced Photon Source. A series of new data analysis techniques were developed to allow quantitative analysis of the x-ray scattering results. The TDS experiments exhibit an excess in the intensity of x-rays scattered to large wavevectors that is consistent with the predicted development of new vibrational modes in membranes with nanometer-scale thicknesses.

Table of Contents

Abstract.....	1
Table of Contents.....	2
Chapter 1: Introduction.....	4
1.1 Acknowledgements.....	5
1.2 Publications Resulting from this Project.....	5
Chapter 2: Background.....	7
2.1: Reciprocal Space.....	7
2.2: Vibrational Phenomena in Solids.....	7
2.2.1: Phonons.....	7
2.3: Phonons in Nanostructures.....	8
2.4: Experimental Probes of the Phonon Dispersion.....	8
2.4.1: Raman and Brillouin Scattering.....	9
2.5: X-ray Thermal Diffuse Scattering.....	9
2.6: Predictions for Silicon Nanomembranes.....	10
Chapter 3: Edge-induced Flattening in the Fabrication of Ultrathin Freestanding Crystalline Silicon Sheets.....	11
3.1: Freestanding Silicon Nanomembranes.....	11
3.1.1: Thermal Diffuse Scattering from Buckled Membranes.....	11
3.1.2: Fabrication Procedure.....	12
3.1.3: Buckling in Silicon Nanomembranes.....	13
3.1.4: Edge-Induced Flattening of Silicon Nanomembranes.....	14
Chapter 4: Thermal Diffuse Scattering as a Probe of Large-Wave-Vector Phonons in Silicon Nanostructures.....	16
4.1: Synchrotron X-Ray Thermal Diffuse Scattering.....	16
4.1.1: Experimental Arrangements.....	16
4.1.2: Experimental Details.....	16
4.2: Analysis of Thermal Diffuse Scattering Data.....	17

4.2.1: Thermal Diffuse Scattering Signature	17
4.2.2: Simulation of Bulk Thermal Diffuse Scattering Signature	17
4.2.3: Determination of Sample Orientation	18
4.2.4: Extraction of Thermal Diffuse Scattering Profiles	18
4.3: Thermal Diffuse Scattering from Silicon Nanomembranes	19
4.3.1: Thermal Diffuse Scattering Intensity Variation with Thickness	19
4.3.2 Excess Thermal Diffuse Scattering Intensity at Large-wavevectors	20
Chapter 5: Future Directions	22
5.1: Further Experiments with Silicon Nanomembranes	22
5.1.1: 3-D Zone Mapping	22
5.3: Calculations of the Intensity of Thermal Diffuse Scattering from a Finite Crystal	23
5.3.1: Initial Derivation of TDS from a Finite Crystal	23
References	26

Chapter 1: Introduction

A unique opportunity arising from the ability to control the nanoscale structure of materials is the potential to modify the modes available for fundamental vibrational excitations of solids by reducing the size of the crystal. In nanostructures, large-wavevector phonons contribute significantly to heat transfer processes because phonons with large-wavevectors are less sensitive to defects and interfaces than small-wavevector phonons.¹ The thermal conductivity and thermoelectric figures of merit are significantly modified in two-dimensional silicon nanomaterials in comparison with their bulk counterparts.^{2–5} In addition, the mobility of electrons in silicon depends on the rate of scattering of electrons between the conduction band valleys mediated by large-wavevector phonons⁶, which have populations and atomic displacements that are modified by reducing the crystal size.^{7,8} The importance of the phonons and their dispersion in silicon and similar nanomaterials has motivated experiments to study phonons in nanoscale volumes.^{9–11}

The spatial periodicity of phonons is defined by their wavevector. The wavevector scale is set approximately by the size in reciprocal space of the silicon Brillouin zone. The boundaries of the Brillouin zone are at wavevectors of approximately $2\pi/a_{\text{Si}}$, where a_{Si} is the Si lattice parameter. Previous experimental and theoretical studies of phonons in silicon nanowires and sheets have been limited to high-energy optical phonons and acoustic phonons with wavevectors smaller than $0.1 \cdot 2\pi/a_{\text{Si}}$.^{12–14} Optical techniques such as Raman and Brillouin scattering have been widely used to probe vibrational phenomena in nanostructures in this small-wavevector regime, but are unable to probe large-wavevector phonons. Scattering with visible light is fundamentally limited due to a mismatch between the momentum of visible photons and the momentum of large-wavevector phonons.¹⁵ The momentum of visible photons is fundamentally on the scale set by the inverse of the visible wavelength λ_{optical} , with values of λ_{optical} on the order of 1 μm . Values of $1/\lambda_{\text{optical}}$ are unavoidably much smaller than $1/a_{\text{Si}}$, which creates a fundamental limitation for optical probes of phonons.

The dispersion of phonons across the entire Brillouin zone is often probed in bulk materials through energy-resolved inelastic scattering techniques such as neutron or inelastic x-ray scattering. X-rays and neutrons have far shorter wavelengths than visible light and thus can be properly matched to phonon wavevectors. Inelastic x-ray and neutron scattering techniques, however, have other experimental limitations. X-rays and neutrons interact relatively weakly with solids and the optics used to define and analyze the probe can be inefficient. As a result of these challenges, inelastic techniques typically require sample volumes of 1 mm^3 or more.¹⁶ Creating well-ordered nanostructures with this volume requirement has proven difficult.

X-ray thermal diffuse scattering (TDS) is an energy-integrated analog of inelastic scattering that allows phonons with wavevectors spanning the Brillouin zone to be probed simultaneously with high momentum resolution. Through the efforts described here, we have demonstrated the ability to probe sample volumes as small as 4 μm^3 , far smaller than energy-resolved inelastic techniques. The cumulative exposure time for our experiments were less than one hour, which has allowed us to make systematic studies of the properties of phonons in silicon nanostructures.¹⁷

We have developed synchrotron x-ray thermal diffuse scattering as a technique for probing the population of phonons in nanoscale systems. The experiments use a model nanoscale system consisting of silicon nanomembranes with thicknesses as small as 4 nm. Phonons in Si nanostructures are relevant in applications ranging from electronics to thermoelectrics. In order to create Si nanomembrane materials suitable for the x-ray scattering studies, we have eliminated a commonly observed buckling instability in semiconductor membranes and fabricated free-standing silicon nanomembranes with unprecedented flatness. The elimination of the buckling instability is crucial because it reduces contributions to the intensity of scattered x-rays that arise from static distortion of the lattice.

Using the x-ray TDS approach, we have probed previously unmeasured large-wavevector phonon modes and observed deviations from bulk TDS intensity distributions. These deviations become systematically more pronounced with decreasing membrane thickness. The magnitudes of the deviations from the bulk predictions are consistent with continuum elastic predictions for small-wavevectors, which predict the development of new mixed longitudinal-transverse character modes. The development of new modes with energies lower than the transverse acoustic mode of silicon by 1-2 meV would be sufficient to account for these large-wavevector deviations.

1.1 Acknowledgements

Parts of this final report are adapted from a document prepared by Kyle M. McElhinny in partial fulfillment of the Research Readiness Exam requirement of the University of Wisconsin's Interdisciplinary Materials Science Graduate Program. Parts of this work were conducted using facilities at the Center for Nanoscale Materials of Argonne National Laboratory. Use of the Center for Nanoscale Materials was supported by the U. S. Department of Energy, Office of Science, Office of Basic Energy Sciences, under Contract No. DE-AC02-06CH11357. Experimental facilities at the University of Wisconsin were partially supported by the National Science Foundation through the University of Wisconsin Materials Research Science and Engineering Center, grant number DMR-1121288.

1.2 Publications Resulting from this Project

The following publications have appeared during the grant period:

1. G. Gopalakrishnan, M. V. Holt, K. M. McElhinny, J. W. Spalanka, D. A. Czaplewski, T. U. Schüllli, and P. G. Evans, "*Thermal Diffuse Scattering as a Probe of Large-Wavevector Phonons in Silicon Nanostructures*," Phys. Rev. Lett., **110**, 205503 (2013).
2. G. Gopalakrishnan, M. V. Holt, K. M. McElhinny, D. A. Czaplewski, and P. G. Evans, "*Probing Large Wavevector Phonons at the Nanoscale via X-Ray Thermal Diffuse Scattering*," Advances in X-ray Analysis, *in press* (2013).
3. G. Gopalakrishnan, D. A. Czaplewski, K. M. McElhinny, M. V. Holt, J. C. Silva-Martinez, and P. G. Evans, "*Edge-induced flattening in the fabrication of ultrathin freestanding crystalline silicon sheets*," Appl. Phys. Lett. **102**, 033113 (2013).

In addition to the papers listed above, two additional manuscripts are planned for submission before the end of 2013. The content of the planned articles is described in Chapter 5 of this report.

Chapter 2: Background

2.1: Reciprocal Space

X-ray scattering results from the interaction between x-rays and the electrons in a sample material. It is convenient when working with x-ray scattering to work in reciprocal (momentum) space. The reciprocal lattice is the set of all wavevectors, \mathbf{G} that yield plane waves with the periodicity of a given Bravais lattice. A wavevector describes the direction and spatial periodicity of waves. The first Brillouin zone defines the region of reciprocal space which is closest to a particular reciprocal lattice point. In this sense the first Brillouin zone is the reciprocal-space analog of the Wigner-Seitz primitive cell in real space. For example, the first Brillouin zone of a BCC lattice is the Wigner-Seitz primitive cell of an FCC lattice. In the case of Si, which has an FCC real-space lattice, the Brillouin zone is a truncated octahedron, shown in orange in Figure 0-1. The black point in the center of the orange truncated octahedron shown in Figure 0-1 denotes the location of the reciprocal lattice point the Brillouin zone is centered around, referred to as the Γ point.

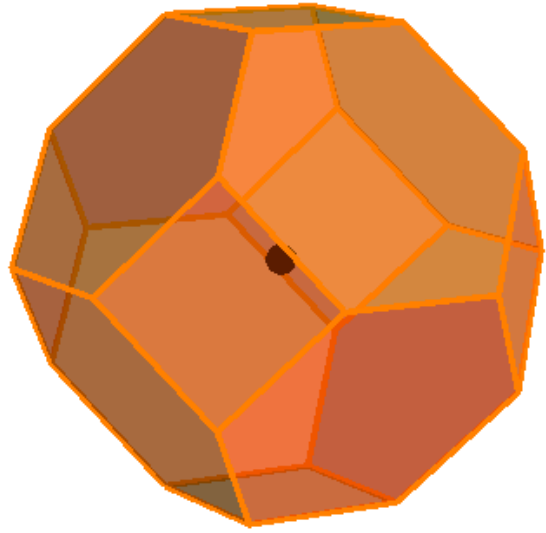


Figure 0-1: The first Brillouin zone of an FCC crystal. The diamond structure of Si is based on the FCC Bravais lattice.

2.2: Vibrational Phenomena in Solids

Vibrational phenomena play an important role in determining the material properties of solids such as its electric, acoustic, elastic and infrared properties. Vibrations also have an important role in phenomena such as superconductivity and phase transformations.¹⁵ Solids are ideally described by a crystal structure in which each atomic site is occupied by an immobile atom. In real crystalline materials, however, the atoms are not fixed in a static lattice, but rather vibrate as a result of the thermal energy in the system. However, a favorable minimization of the elastic potential energy results in a restoring force which limits the magnitude of the atomic displacements. In silicon, the root-mean-square displacement of a thermally excited atom at room temperature is 0.077 Å, corresponding to 1.4% of the silicon lattice parameter.¹⁸

2.2.1: Phonons

Phonons are the fundamental quanta of lattice vibration in solid materials. The states populated by phonons are the elastic normal modes of the crystalline lattice. Each mode is characterized by its wavevector and frequency. Any arbitrary lattice vibration can then be viewed as a superposition of a population of phonons in these normal modes. A plot of the variation of the frequency of the normal modes populated by phonons as a function of their wavevector is called the phonon dispersion.

For a material with a single atom basis, the lattice has three branches of normal modes: two transverse branches and one longitudinal branch. Atoms in a transverse mode have vibrational displacements that are perpendicular to the direction of the wavevector. In a longitudinal mode vibrational displacements are in the same direction as the wavevector. For a material with a two-

atom basis, like silicon, there are a total of six branches: three optical modes and three acoustic modes. The three acoustic modes consist of two branches with transverse polarization and one branch with longitudinal polarization. Similarly there are two transverse optical modes and one longitudinal optical mode. The two transverse branches and one longitudinal branch within a given mode (acoustic or optical) may be degenerate along certain directions depending on the symmetry of the crystal. Acoustic phonon modes have zero frequency at zero wavevector and move the atoms in the unit cell in phase with each other. Acoustic phonons in silicon have energies from 0-50 meV.¹⁹ Optical phonon modes have non-zero frequency at the zero wavevector and move the atoms in the unit cell out of phase with each other. Optical phonons in silicon have energies from 50-70 meV.¹⁹ For reference, the thermal energy at 300 K is 25 meV. The atomic displacements associated with the normal modes of a bulk crystal must be periodic in all spatial dimensions.

2.3: Phonons in Nanostructures

Dimensional confinement of the vibrational modes of solids in nanostructures modifies the electronic, optical, acoustic and superconducting properties of certain structures and devices.²⁰ The dimensional confinement induced by limiting the overall dimensions of the crystal alters vibrational modes and in turn affects the properties they influence. Reducing the size of the crystal leads to confinement-induced modifications of the dispersion of acoustic phonons.^{2,3,21} Confinement-induced changes are also partially responsible for the significant decrease in the thermal conductivity observed in thin films. Decreased thermal conductivity is of particular importance for thermal management of both nanoscale electronic devices, where thermal management is a growing problem, and for thermoelectric materials, where the reduced thermal conductivity serves to increase the thermoelectric figure of merit, ZT .^{2,3} Other phenomena related to acoustic phonons are modified in nanoscale crystals, including the phonon group velocity, the pattern of displacements associated with each mode, and the total density of states.²¹ The decreased phonon group velocity in nanowires and thin films results in increased acoustic phonon relaxation near point defects (vacancies and impurities), dislocations, and phonon-phonon processes.^{21,22}

Optical phonon modes are also different in quantum dots and layered heterostructures than in bulk materials. Electron-phonon scattering rates are influenced by tuning the confined electronic energy states in relation to the optical phonon energy.²³ Optical phonons can also be localized to within individual layers of heterostructures.^{24,25} Technologically important devices are rapidly progressing to smaller dimensions. A fundamental scientific understanding of how phonons are modified by spatial confinement will play an increasing important role in the ability to phonon engineer nanomaterials.

2.4: Experimental Probes of the Phonon Dispersion

The phonon dispersion, $w_s(q)$, can be measured in from experiments in which an external probe exchanges energy with lattice vibrations. Such probes include a beam of neutrons or electromagnetic radiation such as x-rays or visible light. Neutrons and photons probe the phonon dispersion in different ways due to the differing natures of their energy-momentum relationships.

2.4.1: Raman and Brillouin Scattering

Vibrational modes in nanoscale materials have been probed by Raman¹² or Brillouin scattering.^{11,26,27} Optical phonon modes are probed by Raman scattering while acoustic phonon modes are probed by Brillouin scattering. In both techniques, visible photons are scattered by the emission or absorption of phonons. The scattering results in a shift in frequency of 0-1000 cm^{-1} . As with neutron scattering, it is possible to separate one-phonon events from multi-phonon events, allowing the wavevector-frequency relation to be extracted for wavevectors near $q=0$.

There is no size mismatch between optical techniques and nanoscale volumes because of the short absorption length of optical radiation in solids. The interaction between above-bandgap optical radiation and semiconductors occurs over depths of a few hundreds of nanometers, for example. The optics and detectors available for optical light scattering have high efficiency and precision, which allows for the detection of small signals. However, the momentum of an optical photon is on the order of 10^5 cm^{-1} and is thus poorly matched to the dimension of the Brillouin zone which is on the order of 10^8 cm^{-1} . Hence, phonon studies by optical probes are limited to phonons with wavevectors within 0.2% of the zone center.¹¹

2.5: X-ray Thermal Diffuse Scattering

X-ray thermal diffuse scattering (TDS) describes the phenomena associated with the scattering of x-rays by thermal lattice vibrations. Thermal lattice vibrations reduce the intensity of the Bragg peak by the Debye-Waller factor and redistribute the scattered x-rays across broad regions of reciprocal space. The momenta of the x-ray photons used for TDS experiments is on the order of 10^{10} \AA^{-1} , the same order of magnitude as the dimensions of the Brillouin zone. Due to advances in synchrotron sources and x-ray optics small spot sizes with high x-ray flux can be focused on small sample volumes.

Bragg diffraction is characterized by sharp peaks of scattered x-ray intensity in reciprocal space. In a real space picture, Bragg diffraction arises from the constructive interference of x-ray waves scattered from atomic planes. Bragg diffraction occurs when the path length difference between x-rays reflecting from different planes is an integer multiple of the x-ray wavelength. In reciprocal space, the diffraction condition requires that the scattered wavevector q is equal to a reciprocal lattice vector G_{hkl} . The vector G_{hkl} is normal to atomic plane with indices $(h \ k \ l)$ and has a magnitude of $2\pi/d_{hkl}$. Bragg reflections produce sharp intensity peaks in reciprocal space because a Fourier transform relates the real space and reciprocal space structure. The Fourier transform of the infinite real-space lattice is a delta function.

Scattering amplitude from a static lattice can be modified to account for thermal vibration by replacing R_n , the time-averaged mean position, with the instantaneous position term, $R_n + u_n$ where u_n is the displacement from R_n . This replacement leads to the separation of the scattered intensity into two terms. The first term is the elastic scattering from the lattice where the atomic form factor has been reduced by an exponential term known as the Debye-Waller factor. This factor reduces the intensity of the Bragg peak, but does not broaden it. The second term is termed as thermal diffuse scattering (TDS). The intensity of TDS increases with increasing mean-square displacement and it is distributed over a width determined by the correlation of the displacements of its neighboring atoms. Due to the diffuse nature of TDS, the scattering contribution is spread out over large volumes of reciprocal space. Since TDS arises from the instantaneous

displacements of the vibrating it atoms provides information about the population and dispersion of phonons.

TDS is an energy-integrated analog of inelastic x-ray scattering capable of simultaneously probing phonons throughout the entire Brillouin zone. The observed TDS intensity distribution is determined by the phonon dispersion and the polarization of the of the thermally populated phonon modes. The TDS intensity distribution is a direct indication of the phonon population at a given wavevector and temperature. The first-order bulk TDS intensity at scattering wavevector \mathbf{Q} and sample temperature T , is given by:²⁸

$$I(\mathbf{Q}) \propto \sum_j \frac{1}{\omega_j(\mathbf{Q})} \coth\left(\frac{\hbar\omega_j(\mathbf{Q})}{2k_B T}\right) |F_j(\mathbf{Q})|^2 \quad (1)$$

where $\omega_j(\mathbf{Q})$ is the dispersion of the j^{th} phonon branch. The one-phonon structure factor is $F_j(\mathbf{Q}) = \sum_s \frac{f_s}{\sqrt{\mu_s}} \exp(-M_s) [\mathbf{Q} \cdot \mathbf{e}_{j,s}(\mathbf{Q})]$, where f_s and μ_s are respectively the atomic scattering factor and mass of the s^{th} atom in the unit cell, M_s is the Debye-Waller factor, and $\mathbf{e}_{j,s}(\mathbf{Q})$ is the phonon polarization vector. A complete discussion of TDS from an extended solid can be found in ref. 28.

The wavevector \mathbf{Q} in eqn. 1 is the difference between the wavevector of the scattered x-ray \mathbf{S} and the nearest reciprocal lattice vector \mathbf{G} . The intensity observed at \mathbf{S} is determined by phonons with wavevector \mathbf{Q} . This is shown schematically in Figure 0-2. The light-blue streaks of intensity oriented along the z axis are the crystal truncation rods that arise from the broadening of the Bragg peaks due to the finite number of planes contributing the to the Fourier transform along the direction in which the crystal is thin.

Since x-ray TDS measures the population of thermally populated phonon modes it is particularly sensitive to changes in the frequency of the lowest-lying acoustic modes. The modes with energy less than approximately $k_B T$ are highly occupied and contribute to intense thermal diffuse scattering.

2.6: Predictions for Silicon Nanomembranes

The vibrational properties of thin elastic membranes can be described by using elasticity theory in a continuum approximation.²⁹ The solutions resulting from this description have been used to obtain the atomic displacement and phonon frequencies for phonons in the small

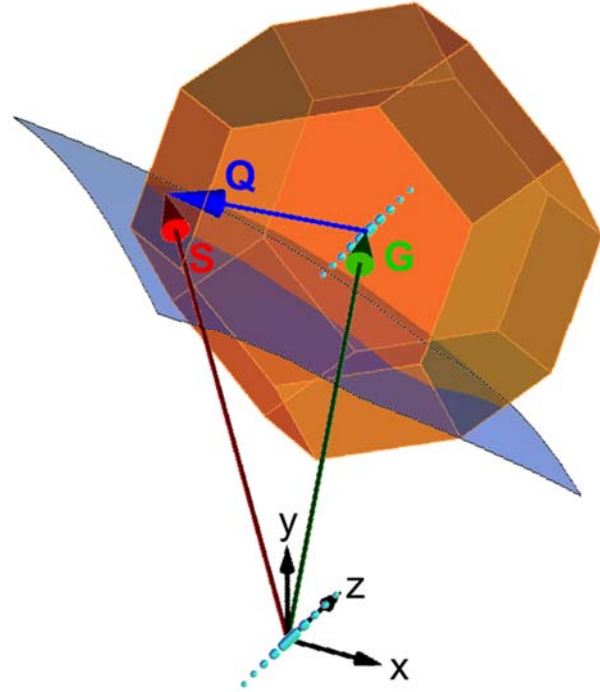


Figure 0-2: First-order thermal diffuse scattering with a momentum transfer \mathbf{S} arises from phonons with wave vector \mathbf{Q} . \mathbf{G} is the reciprocal lattice vector closest to \mathbf{S} . Bragg reflections from silicon membranes are elongated into rods of intensity along the direction normal to the surface of the membrane. The reciprocal-space representation of the x-ray detector (curved blue surface) passes near the zone center and intersects the boundary of the Brillouin zone centered on the (1, 3, -1) reciprocal lattice point (orange polyhedron)

wavevector regime in semiconductor nanostructures.^{2, 18} In the case of thin sheets, the periodic boundary conditions found in bulk systems are replaced by new boundary conditions.

For nanoscale sheets in vacuum, the normal components of the stress must vanish at the free surfaces. This modification of the boundary condition results in the creation of four modes not found in bulk systems: two shear modes (symmetric and anti-symmetric), a flexural mode, and a dilatational mode.³⁰ The flexural and dilatational modes have mixed transverse and longitudinal character. In the case where the membrane thickness is much larger than the characteristic coherence length of the phonons, these modes become a pair of Rayleigh waves localized on the surfaces of the membrane. These flexural and dilatational modes are particularly interesting as their lowest lying modes have phonon frequencies below the lowest lying mode (TA) mode of silicon. A comparison between the bulk Si phonon dispersion and the dispersion of the lowest-lying flexural and dilatational modes is shown in Figure 0-3 (a-b). Figure 0-3 (c) shows the relative magnitudes and direction of the atomic displacements of atoms near the surface of a thin semiconductor sheet for the case of the lowest lying dilatational mode. These low-lying modes contribute over 90% of the TDS intensity, making silicon nanomembranes an interesting system to study.

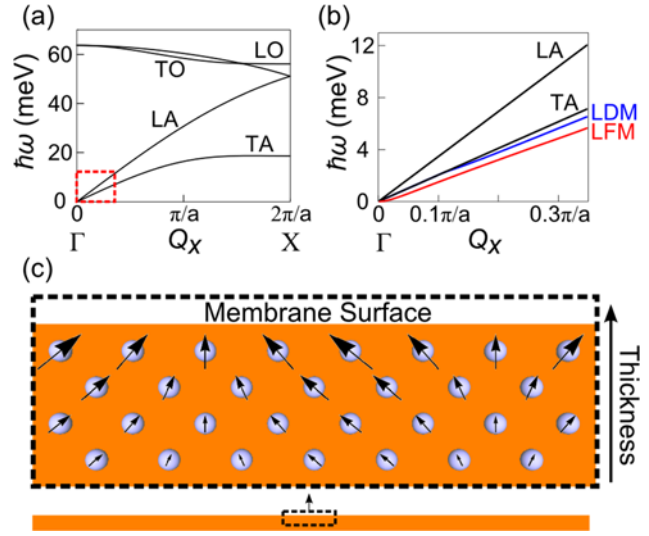


Figure 0-3: (a) Bulk phonon dispersion for Si along the [1 0 0] direction, with transverse acoustic (TA), longitudinal acoustic (LA), transverse optical (TO) and longitudinal optical (LO) branches. (b) Dispersions of the lowest flexural (LFM) and dilatational (LDM) modes of a 10-nm-thick silicon membrane, after Ref. [#], compared with bulk acoustic modes. The energy-wave-vector regime of the comparison is indicated by the red rectangle in the bulk dispersion. (c) Directions and relative magnitudes of near-surface atomic displacements in a Si nanomembrane for an example of the lowest-frequency dilatational mode.

Chapter 3: Edge-induced Flattening in the Fabrication of Ultrathin Freestanding Crystalline Silicon Sheets

3.1: Freestanding Silicon Nanomembranes

In order to study the variation of phonon modes and populations in nanoscale materials we have created freestanding silicon nanomembranes. These are suspended sheets of silicon (Si), with rigidly constrained edges, with areas of $10^4 \mu\text{m}^2$ and thicknesses less than several hundred nanometers. We chose silicon nanomembranes to study the effects of nanostructuring on vibrational phenomena because silicon has well understood fabrication methods and a large number of calculations and theoretical predictions with which we could compare our results.

3.1.1: Thermal Diffuse Scattering from Buckled Membranes

Extracting information about the population, energy, and momentum of phonons by x-ray thermal diffuse scattering requires a well-ordered single-crystalline sample of known orientation.

Single-crystal silicon systems satisfy both of these requirements. However, silicon nanomembranes fabricated from silicon-on-insulator materials, as was done in our work, commonly suffer from a buckling instability when the membrane is released from the substrate.^{31–35}

Our initial TDS experiments were performed on buckled membranes however the static scattering originating from the crystal misorientation generated by the buckling was sufficient to obscure the relatively weak scattering TDS intensity distribution.³⁶ A detailed description of the experimental setup for TDS measurements from nanomembranes is given below in Chapter 4. At this point it is sufficient to know that the distortion of the buckled membrane produces diffuse scattering from strain gradients that competes with the TDS signal. Intensity distributions of a flat 44 nm-thick membrane (Figure 0-1(a)) and a buckled 60 nm-thick membrane (Figure 0-1 (b)) are shown in Figure 0-1. In both Figure 0-1(a) and (b) the beam is passing through the membrane, as indicated by the presence of truncation rod observed on the left side of the image. In (b) however, the TDS signature, presented in (a) as a green oval and faint streak extending towards the upper corner of the image, is obscured by diffuse static scattering, which is most intense in the lower right corner of (b).

To resolve the weak TDS scattering signature, it became necessary to eliminate the buckling of the Si nanomembranes. The process we developed to flatten the membranes is termed *edge-induced flattening*.³⁶ This method utilizes the relative interfacial energies of water-Si, air-Si, and Si-Si during the drying process to flatten and maintain the membrane in a metastable flattened state. The compressive strain in the membrane previously relieved by buckling is confined to the edges of the membrane. This results in a flat, tensile-strained central region of the membrane. Silicon membranes from 315 nm to 4 nm have been fabricated by this procedure, with vertical deviations below 10 nm over a central 100 μm x 100 μm area.³⁶

3.1.2: Fabrication Procedure

Membranes were fabricated using [100]-orientated silicon-on-insulator (SOI) as a starting material. The structure of the SOI (Figure 0-2 (a)) consisted of device layers of varying thicknesses, buried oxide

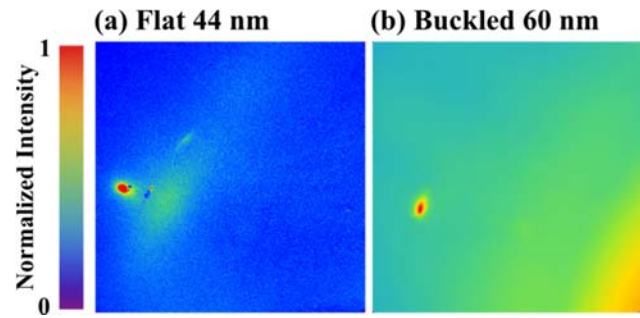


Figure 0-1: X-ray diffuse scattering patterns acquired from (a) a flat 44 nm-thick silicon nanomembrane and (b) a 60 nm-thick buckled membrane. The static scattering intensity originating from the buckling in (b) is large enough to obscure the comparatively small thermal diffuse scattering signature observed in (a).

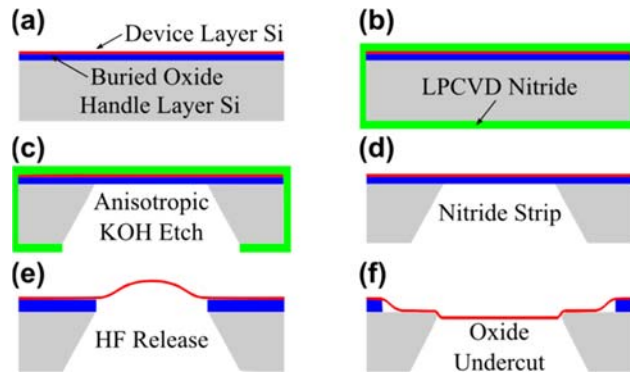


Figure 0-2: Schematic of silicon nanomembrane fabrication. (a) Starting SOI structure (b) Protective layer of SiN deposited by LPCVD. (c) Formation of membrane window by lithographic patterning and an anisotropic KOH etch. (d) Removal of SiN by H_3PO_4 etch. (e) Membrane release by dissolving the buried oxide in the window, resulting in a buckled structure. (f) Undercutting the buried oxide layer by etching past the edges of the windows, resulting in a flattened structure.

layers with thicknesses less than 1 μm , and [100]-oriented 625 μm -thick silicon handle wafer. Membrane fabrication was carried out in the clean room facilities at the Wisconsin Center for Applied Microelectronics and at the University of Wisconsin-Madison and in collaboration with the Center for Nanoscale Materials (CNM) at Argonne National Laboratory. The SOI wafers were cleaned using a standard pre-furnace clean of acid piranha, SC1, SC2 and a final hydrofluoric acid (HF) dip. The SOI device layer was then thinned by wet thermal oxidation at 950°C. Oxidation time was chosen using the Deal-Grove model for oxidation, with the assumption that the thickness of silicon consumed during the oxidation was equal to 45% of the final thickness of the silicon dioxide layer. After oxidation, the SiO_2 layer was removed using HF and the thickness was measured using a reflectometer.

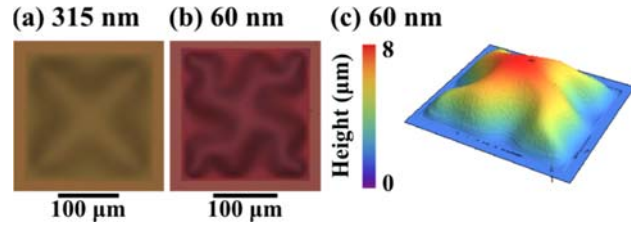


Figure 0-3: Optical micrographs of buckled silicon nanomembranes with thicknesses of (a) 315 nm and (b) 60 nm. (c) Height map of the 60 nm membrane obtained by white light interferometry.

While the sample is still hydrogen terminated from the HF dip, a 200 nm-thick coating of non-stoichiometric, low-stress silicon nitride (SiN) is deposited on the sample by low-pressure chemical vapor deposition (LPCVD) at 850°C (Figure 0-2 (b)). The SiN layer is used as both an etch mask for the subsequent backside etch as well as a protective layer to protect the device layer from etching during the remainder of fabrication. Next, the back side of the handle wafer is patterned using UV lithography, and the exposed regions of the SiN are removed using a reactive ion etch (RIE) of $\text{CF}_4 + 10\% \text{O}_2$ at 60 mTorr, for 10 minutes. The membrane window is then created by using an anisotropic potassium hydroxide (KOH) etch which results in a trilayer window of $\text{SiO}_2/\text{Si}/\text{SiN}$, 200 $\mu\text{m} \times 200 \mu\text{m}$ in dimension (Figure 0-2 (c)). KOH has favorable etch selectivity for Si (1.4 $\mu\text{m}/\text{min}$ at 94°C) over SiN ($< 1 \text{ \AA}/\text{min}$) and SiO_2 (14 $\text{ \AA}/\text{min}$). This allows the KOH etch to be stopped when it reaches the BOX layer. However if the etch depth is not monitored during etching, the KOH can etch through the BOX layer and quickly etch the device layer. This monitoring is necessary as the etch rate decreases over time due to the reduced kinetic transport of KOH and H_2O molecules into the etch area. Typically, an eight hour KOH etch at 94°C followed by a two hour etch at 84°C is used to etch through the 625 μm handle wafer and stop at the BOX layer.

The SiN layer is then removed using a phosphoric acid (H_3PO_4) etch at 160°C (Figure 0-2 (d)). The thickness of the device layer Si is reduced by 1-4 nm from the value measured before the SiN deposition. At this point, the device layer silicon is still bound by the BOX layer beneath it. A membrane is formed by releasing the device layer silicon from BOX layer by removing the BOX layer in the window using HF (Figure 0-2 (e)). Procedures similar to the one described above have been used to fabricate membranes from with thicknesses ranging from several microns^{37,38} to tens of nanometers.^{26,27,32,34,39-44}

3.1.3: Buckling in Silicon Nanomembranes

The buckled structure observed in Figure 0-2(e) is commonly observed in semiconductor membranes, particularly membranes fabricated from SOI. Before the BOX layer is etched away, the BOX layer constrains the device layer, preventing it from elastically relaxing any stored strain energy. The stored strain energy originates from a residual compressive stress in the device layer generated during the SOI and membrane fabrication. When the BOX layer is removed from

within the membrane window, the device layer silicon in the window is no longer constrained and it assumes its lowest energy conformation, the observed buckled structure. Figure 0-3 shows the buckling patterns generated for a (a) 315 nm and (b) 60 nm-thick membrane. The geometry of the patterns are determined by the ratio of thickness and lateral dimensions.⁴⁵ A height map of the vertical displacement of the 60 nm-thick buckled membrane is shown in Figure 0-3(c). The maximum vertical displacement is 7.8 μm , which corresponds to a curvature of $1.5 \times 10^{-3} \mu\text{m}^{-1}$. The height profile map is used to estimate the magnitude of the initial compressive strain in the device layer by measuring the increase in length of a line along the profile of the buckled membrane and comparing it to the expected horizontal length. For the 60 nm-thick membrane shown in Figure 0-3(c), the excess length along a path which passes through the midpoint of the buckled membrane is measured to be 0.74 μm , corresponding to a compressive strain of 0.37%. This is consistent with elastic continuum approximations for the primary buckling amplitude and with previous reports.⁴⁶

3.1.4: Edge-Induced Flattening of Silicon Nanomembranes

To create flattened silicon nanomembranes suitable for x-ray scattering measurements, a new fabrication procedure termed “edge-induced flattening” was developed. During the HF release step, the BOX layer is etched not only directly within the membrane window, but also in an area approximately 30 μm past the edges of the window in every direction (Figure 0-4 (a)).

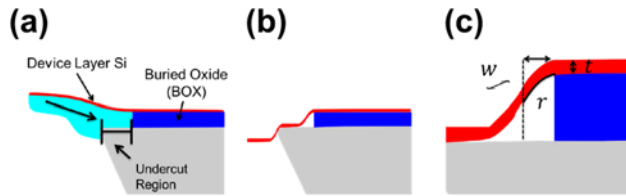


Figure 0-4: Schematic of the undercutting and edge induced flattening mechanism. (a) Schematic of flattening process. The membrane dries from the center of the membrane, pulling the central portion of the membrane flat. (b) The final geometry along the edge of a flattened membrane. The geometry is maintained by the large Si-Si contact area along the edges. (c) Schematic of variables used in calculating bending energy along the edge.

The membrane is then cleaned in deionized water.

To minimize the probability of membrane rupture during the rinsing and drying process the membrane is passed through the water-air interface at an oblique angle so as to minimize the interfacial forces. As the membrane dries, the water on the backside of the membrane dries from center of the membrane out toward the edges (Figure 0-4 (a)). Then as the water recedes down etch walls, it brings the device layer Si into contact with the handle wafer Si, creating a large Si-Si

contact area. The resultant structure is a flat central region of the membrane, which is held in tension, with a sharply bent region near the edge of the membrane (Figure 0-4(b)). The tensile strain in the membrane is confirmed by Raman measurements.

Membranes fabricated using the edge-induced flattening procedure are shown in Figure 0-5 (a)-(d). Figure 0-5 (e) shows a height profile map, acquired by white-light interferometry, of the 6 nm-thick membrane shown in (d). The height profile map reveals narrow regions along the edges of the membrane where the buckling is concentrated (Figure 0-6 (a)). Additionally, it shows a central 100 μm region where the vertical deviation of the membrane is less than 10 nm (Figure 0-6 (b)). This demonstrates a reduction in the radius of curvature of the membrane of over three orders of magnitude from the original buckled membrane.

The formation of flat membranes via this process is favorable as a result of the relative energies of the water-Si, air-Si, and Si-Si interfacial energies. As the water recedes from the center of the membrane, the water-Si contact area will be maximized as the water-Si interfacial energy ($10^{-13} \text{ J}/\mu\text{m}^2$) is more favorable than the air-Si interfacial energy.⁴⁷ The energy contribution of the water-Si interface is especially large, 10^{-10} J , due to the large area ($10^3 \mu\text{m}^2$) that the interface covers along the edges of the membrane. The maximization of the contact area during drying causes the excess length in the membrane to be pushed to the sides of the membrane and creating a flat, tensile-strained central region. The maximum excess length which can be confined to the edges is two times the thickness of the BOX layer. As the water continues to recede down the etch walls of the window, it brings the device layer Si into contact with the freshly exposed handle wafer Si. The Si-Si interfacial energy is estimated to be $10^{-13} \text{ J}/\mu\text{m}^2$ but is subject to local deviations caused by surface roughness and local differences in surface chemistry. This energy is sufficient to bond the device/handle Si interface together along the edges of the membrane and maintain it in a metastable flattened state.

In order for the edge-induced flattening mechanism to work, the interfacial energies of both the drying and interfacial bonding processes, both estimated to be 10^{-10} J , must be larger than the energy penalty incurred by confining the excess length to a localized region of high curvature near the edges of the membrane. The elastic energy stored in the curved regions along the edges of the membrane is estimated by treating the membrane edge as a beam of width w and thickness t . The beam is then considered to be bent with a mean radius of curvature r as shown in Figure 0-4(c). The radius of curvature was estimated though by optical interferometry. The strain energy from bending is proportional to:

$$U_{\text{strain}} \propto E \times \frac{t^2}{r^2} \times lwt = \frac{Elwt^3}{r^2}$$

Where E is the elastic modulus of flexure, and l is the length of the beam.

For a 30 nm-thick membrane, the total strain energy in the edge regions is 10^{-12} J , two orders of magnitude smaller than the energy gained by creating both the water-Si and then the Si-Si interfaces. Membranes flattened by this procedure have been shown to be suitable for x-ray scattering measurements.

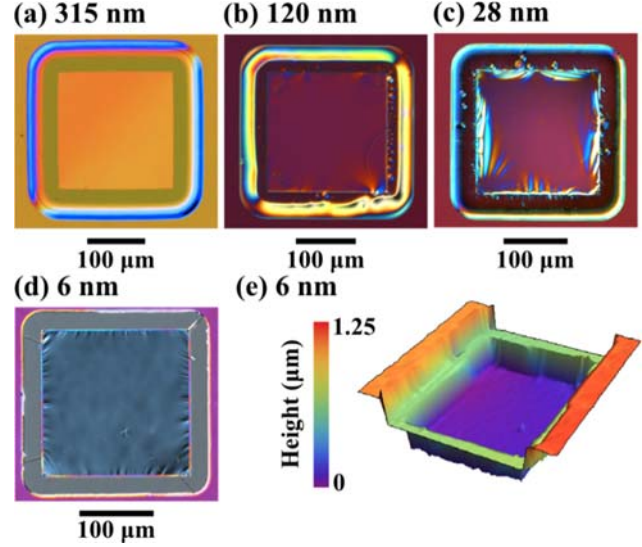


Figure 0-5: (a)-(d) Optical micrographs of flat membranes fabricated via the undercut etch procedure, with thicknesses as indicated. (e) Height map of the 6 nm-thick membrane surface obtained by white light interferometry.

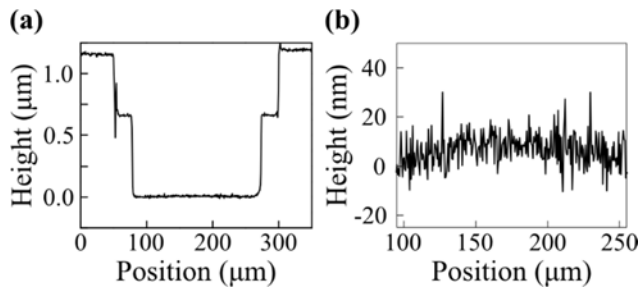


Figure 0-6: (a) Height profile of the 6 nm-thick membrane along a line passing through the center of the membrane area, horizontal with respect to the micrograph in Fig.3(d). (b) Magnified line profile along the center of the suspended membrane, showing the short- and large-scale variations in the membrane height.

Chapter 4: Thermal Diffuse Scattering as a Probe of Large-Wave-Vector Phonons in Silicon Nanostructures

4.1: Synchrotron X-Ray Thermal Diffuse Scattering

4.1.1: Experimental Arrangements

Synchrotron x-ray thermal diffuse scattering measurements were carried out at station 26-ID-C of the Advanced Photon Source (APS) at Argonne National Lab. A schematic representation of the experimental setup is shown in Figure 0-1. The measurement was performed in a transmission geometry, with the plane occupied by the silicon nanomembrane normal to the incident beam. The samples were mounted in a vacuum chamber in order to minimize the contribution of air scattering to the scattered intensity. A 10-keV x-ray beam was focused on the membrane with a 30 μm spot size using a capillary condenser. Contributions from unfocused or secondary x-rays were minimized by utilizing a 150 μm order sorting aperture placed along the beam path between the condenser optic and the sample. A lead (Pb) beam-stop was positioned downstream of the sample to absorb the portion of the direct beam which passed through the sample. Lead shielding was shaped into a truncated pyramid extending from the beryllium exit window of the evacuated chamber to the sample. The shielding was positioned in the chamber to eliminate the scattering contributions of scattered x-rays which did not originate from the sample, such as scattering from optics and other surfaces inside the chambers. X-rays scattered by the sample were detected using a charge-coupled device (CCD) (Mar Inc.) with a pixel size of 80 μm and a total diameter of 165 mm. The detector subtended a conical angle of approximately 15° .

The sample orientation was chosen to avoid exciting Bragg reflections and to capture the TDS signal from wavevectors ranging from about $0.1(2\pi/a_{\text{Si}})$, representing points near the zone center, to $2\pi/a_{\text{Si}}$, corresponding to points on the zone edges, where a_{Si} is the Si lattice parameter, 5.431 Å.

4.1.2: Experimental Details

Thermal diffuse scattering intensity distributions were collected from a series of membrane samples with thicknesses between 315 nm and 6 nm. Intensity distributions from the surrounding bulk support structure were also acquired for comparison and to aid in determining the sample orientation. Background measurements were performed by mechanically removing the membrane from a window of a sample and passing the incident x-ray beam through the open window. These background images allowed non-sample sources of scattering to be subtracted from the sample data to obtain

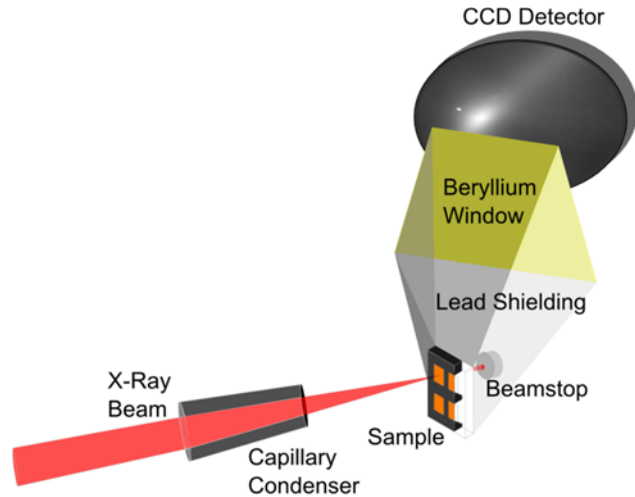


Figure 0-1: Schematic representation of the experimental setup for nanomembrane TDS measurements at 26-ID-C of the Advanced Photon Source (APS). All components except the CCD Detector reside within an evacuated vacuum chamber during the measurement to reduce scattering from air.

an accurate measurement of the TDS intensity without contamination from static scattering sources. Exposure time varied, depending on sample thickness. The exposures were double-correlated to eliminate zingers, random events from cosmic rays or from the decay of radioactive isotopes with the detector. Sets of two to three scans, with a cumulative exposure time of approximately one hour were required to resolve the weak TDS signature from phonons near the zone boundaries. These scans were averaged and an average of background scans from a mechanically removed window of the same orientation was subtracted to show only the x-rays scattered by the sample.

4.2: Analysis of Thermal Diffuse Scattering Data

4.2.1: Thermal Diffuse Scattering Signature

The scattering signature of the TDS from a 315 nm-thick membrane is shown in Figure 0-2. The isolated, sharp, bright, oval spot on the left of the detector is the intersection of the reciprocal space sheet corresponding to the detector plane with Si crystal truncation rod, which replaces the Bragg peak when diffracting from two-dimensional systems. To the right of the crystal truncation rod is the region of maximum TDS intensity. The intense feature in the image arising from the truncation rod corresponds to the point on the detector which lies closest in reciprocal space to the center of the Brillouin zone.

Since TDS is sensitive to the population of thermally populated phonons, and the phonon population is highest near the zone center, the TDS intensity will be greater when the Ewald sphere passes closer to the zone center. The orange lines shown on the image are the intersections of the edges of the Brillouin zone centered on the (1,3,-1) reciprocal lattice point, with section of the Ewald sphere caught by the detector plane. Additionally, a diagonal streak of intensity extends from the region of maximum TDS intensity diagonally toward the upper right region of the image. This corresponds to a path which roughly follows the path from the gamma point in the center of the Brillouin zone to the X point on the zone boundary. TDS intensity is expected to be higher along this path due to the elastic anisotropy of Si. The quantity called Q_x is the projection of the phonon wavevector, Q , onto the x axis, [100], of reciprocal space. Values of Q_y and Q_z along this streak are less than $0.25 \cdot 2\pi/a$ and do not deviate greatly over the length of the streak.

4.2.2: Simulation of Bulk Thermal Diffuse Scattering Signature

The TDS intensity distribution expected from using the bulk Si phonon dispersion was computed using the equations given above. The bulk Si phonon dispersion used in the calculations was computed by utilizing the dynamical matrix for Si, which is the Fourier transform of the force constant matrix. The matrix can be constructed and diagonalized for any wavevector in the Brillouin zone,

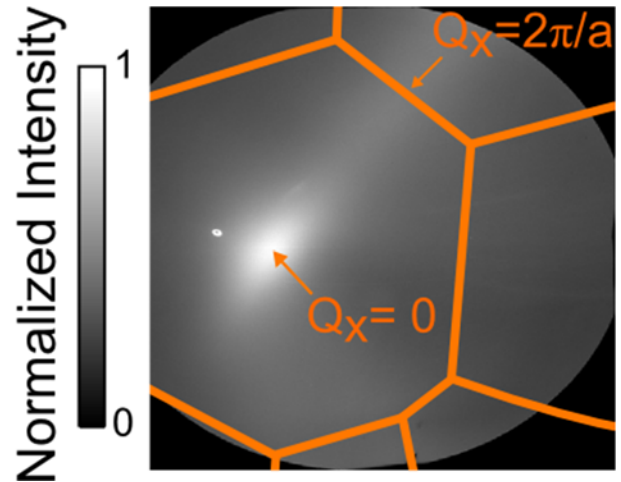


Figure 0-2: TDS intensity distribution from a 315 nm-thick silicon nanomembrane. The intersections of the Brillouin zone edges with section of the Ewald sphere caught by the detector plane are shown as orange lines.

which can be used to extract the phonon dispersion.¹⁹

Then the region of reciprocal space being probed by the beam is computed using the beam energy and geometric considerations. The sample θ , ϕ , and ψ are accounted for as well as the location of the detector. The value of the scattering wavevector q for each pixel is then computed.

The expected TDS intensity for each pixel is then computed using its associated position in reciprocal space. An example of a simulated image is shown in Figure 0-3. The white regions indicate areas of high intensity. The red, green, and blue lines represent lines of constant q_x , q_y , and q_z , respectively. The intersection of the red and green (q_x and q_y) lines indicate the position of the intersection of the Si crystal truncation rod with the detector plane.

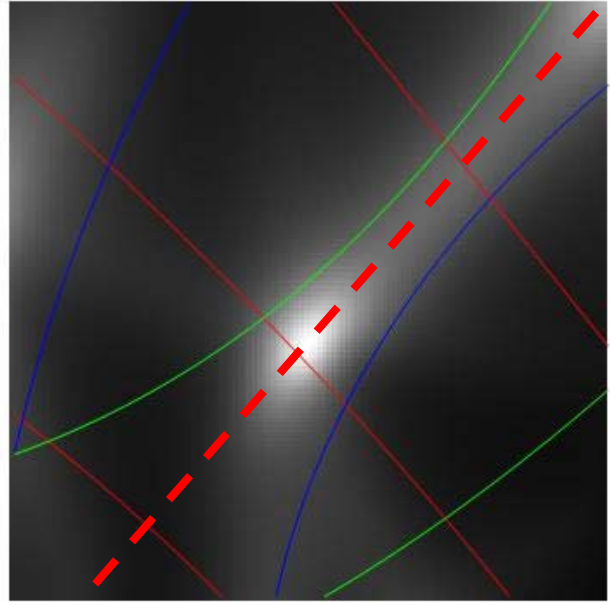


Figure 0-3: Simulation of the expected TDS Intensity. White regions indicate areas of high intensity. The red, green, and blue lines represent lines of constant q_x , q_y , and q_z , respectively. The intersection of the red and green (q_x and q_y) lines indicate the position of the intersection of the Si crystal truncation rod with the detector plane. The dashed red line is the path along which profiles were extracted.

4.2.3: Determination of Sample Orientation

A slight misorientation of the sample in the θ , ϕ , and ψ angles occurs during its mounting onto the sample holder and from inaccuracy in the sample adjustment. As a result, the exact orientation of the sample in the beam is not known. Additionally, in our initial experiments, the exact location of the detector was not known. In later experiments, the detector position was fit experimentally by matching the powder diffraction pattern of Si from a sample mounted in the same location as the membrane sample. In order to determine the sample orientation and detector locations, simulated detector images, generated by changing the sample θ , ϕ , and ψ and detector height above the beam and angle from the beam, were compared to experimentally measured bulk and membrane samples.

The x and y pixel locations of the truncation rod and the maximum in TDS intensity were used as indicators of agreement between the simulated image and the experimental image. Changing the detector angle resulted in only a horizontal change in pixel number, corresponding to the x pixel value. Changing the detector height resulted in an only vertical change in pixel number, corresponding to the y pixel value. For determining sample θ , ϕ , and ψ , three new parameters were used, the distance and the angle between the location of the truncation rod and maximum in TDS intensity, and the angle at which the high streak of intensity which goes from the maximum in the TDS is at. When these three parameters were satisfied, the image could be translated using the detector location to generate a matching image. The approximate values of sample θ , ϕ , and ψ are known initially from the experimental setup.

4.2.4: Extraction of Thermal Diffuse Scattering Profiles

TDS profiles were extracted along a path which passes through the maximum in the TDS intensity and extends along the streak of high intensity. Profiles were extracted using a

Mathematica notebook. The profiles were calculated by extracting a rectangle of pixels 51 pixels wide and 2048 pixels long. Columns of 51 pixels were averaged into a single value. The 2048 pixels were then averaged via a moving average with a window width of 71 pixels to create the profiles shown later in this chapter.

4.3: Thermal Diffuse Scattering from Silicon Nanomembranes

The experimental setup was tested by collecting x-rays scattered from a bulk region near the membrane sample. The collected pattern was compared to the pattern expected from TDS theory using the bulk Si phonon dispersion. The comparison is shown in Figure 0-5. Figure 0-5 (a) shows the experimentally observed bulk TDS pattern and (b) shows the predicted pattern. Figure 0-5 (c) shows an intensity profile extracted along the paths indicated in (a) and (b), which traverse from near the zone center to near the zone edge. The profiles are scaled using a single multiplicative scaling factor to match the observed and predicted TDS profiles. The images and extracted profile show good agreement between the observed and predicted TDS. TDS scattering patterns from Si nanomembranes with thicknesses of 315, 44, 28 and 6 nm are shown in Figure 0-4 (a)-(d). The intensity in the image is normalized to the highest value, which is the truncation rod. Membranes with reduced thicknesses show a lower TDS intensity and what appears to be a relative increase in the intensity of the truncation rod.

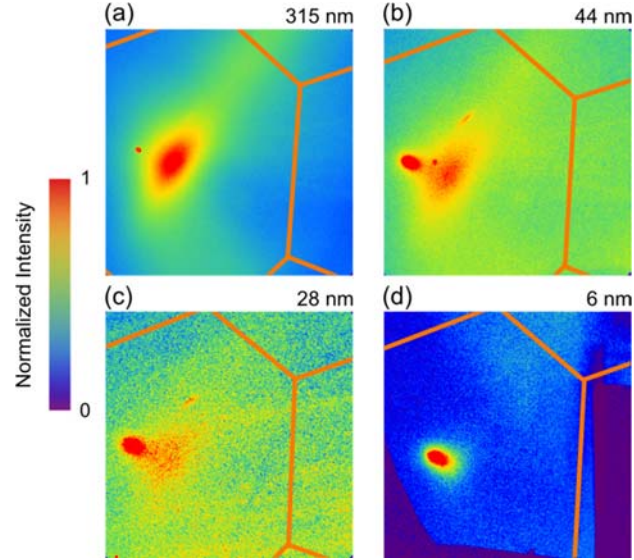


Figure 0-4: (a)-(d) Nanomembrane thermal diffuse scattering intensity distributions for membranes with thicknesses of 315, 44, 28, and 6 nm, normalized to the TDS intensity maximum in each image. The bright spot to the left of the maximum in the diffuse scattering arises from the crystal truncation rod. Orange lines represent zone boundaries.

4.3.1: Thermal Diffuse Scattering Intensity Variation with Thickness

The first result is that the TDS intensity varies linearly with thickness in the nanometer regime. Figure 0-6(a) shows the expected scaling of TDS of silicon up to a thickness of a few hundred microns. The maximum in intensity occurs at the x-ray attenuation length of silicon. The plot indicates the expected linearity of TDS intensity with thicknesses in the sub-micron thickness regime. Figure 0-6(b) and (c)

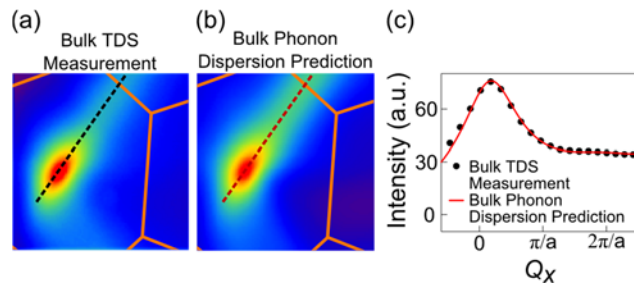


Figure 0-5: (a) Experimentally observed TDS intensity for a bulk-like thickness of the SOI handle wafer. (b) Predicted first order TDS intensity based on the bulk phonon dispersion (c) Intensity profile of the measured TDS intensity (points) and TDS predicted from the bulk Si phonon dispersion (line) along the paths indicated in (a) and (b).

show the variation in TDS intensity as a function of thickness in the Si nanomembrane samples. The variation is shown at two different, representative points in reciprocal space, one from near

the zone center (b) and one from near the zone boundary (c), with $Q_x = 2\pi/a_{Si}$. Sample-to-sample intensity variations in the small thickness regime arise partially due to the small deviations in sample orientation generated by the sample mounting procedure. This causes the path sampled in reciprocal space to be slightly different, passing either closer or farther from the zone center resulting and intensity dependence on sample orientation as well as thickness.

4.3.2 Excess Thermal Diffuse Scattering Intensity at Large-wavevectors

For thicker membranes, such as the 315 nm-thick membrane, the TDS intensity distribution closely matches the bulk intensity distribution with a slight deviation observed near the zone edge. The deviation near the zone edge becomes more apparent and pronounced with decreasing membrane thickness, such as the 44 and 28 nm-thick samples. In the thinnest membranes, such as the 6 nm-thick sample, the TDS signal at large wavevectors coincides with a large scattering contribution from the residual, un-subtracted background and static scattering from the oxide layer.

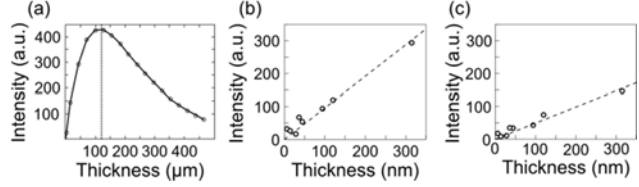


Figure 0-6: (a) Expected thickness scaling of x-rays TDS for samples in the few hundreds of microns region. The maximum in TDS intensity occurs at the attenuation length of Si

The deviation in the TDS intensity observed from silicon nanomembranes samples is apparent in the dependence of the TDS intensity on the wavevector component Q_x . Figure 0-7 (a)-(d) (black dots) shows the dependence of TDS intensity on Q_x . The profiles are extracted along the high intensity streak extending from the maximum in the TDS intensity towards the right corner, along the path shown in Figure 0-3. This corresponds to a reciprocal space path which starts near the zone center and extends along the high symmetry Γ to X direction. The red squares correspond to a profile taken from a bulk region near the membrane sample to which they are being compared. The membrane and bulk profiles are normalized to unity at their peak intensity of one, and offset for clarity. A broad excess in the TDS intensity is easily observed in these profiles between $Q_x = 3/2 \pi/a_{Si}$ and $2\pi/a_{Si}$.

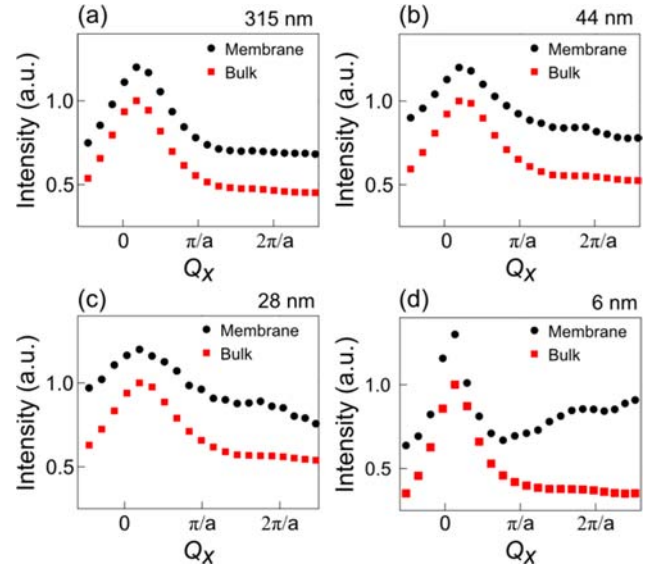


Figure 0-7: Dependence of the TDS intensity on the wave vector Q_x for (a) 315, (b) 44, (c) 28, and (d) 6 nm membranes (black circles) and for bulk-like regions of the SOI handle wafer for each sample (red squares). The intensity profiles are normalized to unity at their maxima and offset vertically for clarity. The central maximum in (d) is sharper than in thicker samples due to a small difference in the sample orientation.

In a very simple model, the excess intensity at large wavevectors can be accounted for by modifying the phonon energy at those wavevectors. A confinement-induced reduction in the phonon energy by as little as 1-2 meV would be sufficient to yield an increase of 10% in TDS intensity at large-wavevectors. This would be consistent with previous results where confinement energies

on the order of 0.5 meV in 30-nm-thick membranes have been established in the small-wavevector regime.²⁶ While these deviations are consistent with the energy scale of these previous results, they occur at larger wavevectors at which different modes of vibration are relevant. We thus stress that the results are consistent with the development of the new modes, but that full quantitative comparison is not yet possible.

The predicted phonon dispersions of nanomembranes available in the literature are based on elasticity theory, as discussed in section 2.6. The continuum elastic approximation limits these calculations to long wavelength modes for which the length scale imposed by atomic bonding is irrelevant. A more detailed comparison of the experimental results with theory will require the computation of phonon dispersions based on atomistic rather than continuum theories. Such predictions yield similar large-surface-displacement vibrational modes with very low frequencies in Si nanowires,⁴⁸ but are not yet available for Si membranes with thicknesses of many nanometers.

In summary, the deviations from bulk TDS intensities observed here at large-wavevectors suggest that the dispersion of large-wavevector phonons in silicon membranes with thicknesses in the tens of nanometers and smaller is substantially different than in bulk Si. This is important because phonons in this regime are thermally relevant in silicon nanostructures because the longer-wavelength, small-wavevector phonons are efficiently scattered at boundaries and contribute less to thermal conduction at the nanoscale.⁵ Similar modes are also electronically relevant to the inter-valley-scattering-limited electron mobility of lightly doped silicon.

Chapter 5: Future Directions

5.1: Further Experiments with Silicon Nanomembranes

5.1.1: 3-D Zone Mapping

In the experiments detailed in Chapter 4, TDS intensities were extracted along a single arbitrary path in reciprocal space that followed the curve of the Ewald sphere and then subsequently plotted as a projection of the phonon wavevector on the reciprocal space x-axis. In order to extract TDS, and hence phonon, information along the any direction in the crystal, particularly the high-symmetry directions, we performed a measurement in which a series of x-ray scattering exposures were acquired to acquire a map of the intensity across a full 3-D Brillouin zone. The sample was oriented such that a rotation in θ over a range of 45 degrees would sweep the detector plane through the full Brillouin zone in increments of 5 degrees of rotation. The experimental design is shown schematically in Figure 0-1 (a). This procedure populates a 3-D array of points within the Brillouin zone, shown in Figure 0-1(b). Intensity profiles can then be extracted along arbitrary directions by looking at points from each “slice” which fall within a particular range of Q . We for example have analyzed the data by creating slices for which the points less than $0.05 \, 2\pi/a_{Si}$ from a particular rod are averaged together. Preliminary analysis of these profiles indicate a modification of the TDS intensity in the [001] direction, the direction expected to be modified by the spatial confinement in that direction. These results are planned for publication in Fall 2013.

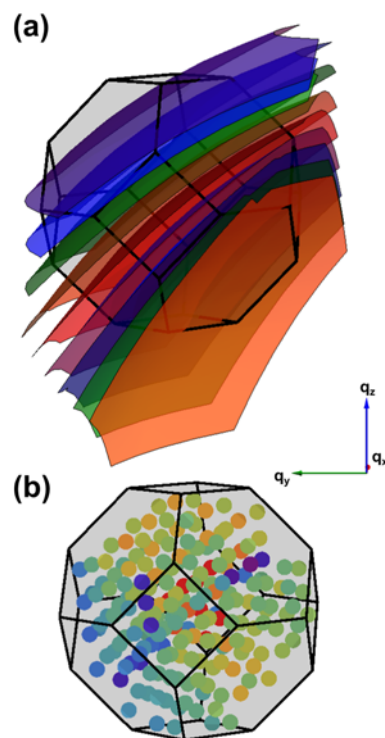


Figure 0-1: Schematic of the 3-D zone mapping experiment. (a) The portion of the Ewald sphere captured by the detector, displayed as multicolored planes. The planes start at a sample theta of approximately -15 degrees and move towards +30 degrees from bottom to top. (b) The first Brillouin zone of silicon centered on the (1,3,-1) reciprocal lattice point populated by colored spheres indicating the TDS intensity at the Q within the Brillouin zone.

5.2: Other Materials and Structures

5.2.1: SiGe Nanostructures

In an effort to expand TDS measurements beyond Si nanomembranes, Si/SiGe/Si trilayer membranes were fabricated and measured using the same TDS experimental arrangement. In order to facilitate TDS studies, the sample fabrication procedure described in Chapter 3 was modified. The SOI starting material was

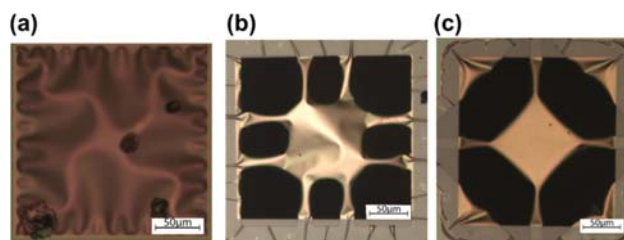


Figure 0-2 (a) an unpatterned Si/SiGe/Si trilayer displaying a characteristic buckling pattern (b) the patterned trilayer using an 8 arm pattern (c) the trilayer patterned using a 4 arm pattern. The 4 arm pattern shows the improvement in membrane flatness.

thinned such that the device layer was 20 nm-thick. A 20 nm-thick layer of Si_{0.75}Ge_{0.25} was grown on top then capped by a 20 nm-thick Si layer, via chemical vapor deposition. This trilayer membrane structure was then processed as described in Chapter 3. However, due to strain effects arising from the lattice mismatch between SiGe and Si the edge- induced flattening procedure cannot remove all of the strain. Further flattening of the membrane was accomplished by strain-relief patterning. Strain relief structures consisting of arms and a central square region were patterned inside the membrane window. Unpatterned and patterned membranes can be seen in Figure 5.2. The pattern shown in Figure 0-2 (c) reduced the maximum curvature of the membrane within the x-ray spot by 81%, allowing for x-ray studies to be performed. TDS patterns were observed from the trilayer structure. We plan to publish these results in Fall 2013.

5.3: Calculations of the Intensity of Thermal Diffuse Scattering from a Finite Crystal

A key component in extracting the phonon dispersion from a finite crystal such as a nanomembrane or nanowire is to develop the expected intensity distribution formulae for finite sized objects. During the derivation of the bulk TDS theory, several assumptions are made which require the approximation of an infinite lattice, an assumption which is invalid in the finite crystal. A preliminary derivation without these assumptions is outlined in the following pages. Results of this initial derivation result in the generation of a position dependent Debye-Waller factor and a modulation of the atomic displacements by the confinement in the thickness direction. In the limiting case of an infinite crystal, the derived expressions simplify to their bulk TDS counterparts.

5.3.1: Initial Derivation of TDS from a Finite Crystal

The scattering amplitude from a lattice is $A(\mathbf{Q}) = f(\mathbf{Q}) \sum_n e^{i\mathbf{Q} \cdot \mathbf{r}_n}$, where $f(\mathbf{Q})$ is the atomic scattering factor at wavevector \mathbf{Q} . The scattered intensity is:

$$I(\mathbf{Q}) = A^*(\mathbf{Q})A(\mathbf{Q}) = |f(\mathbf{Q})|^2 \sum_{m,n} e^{i\mathbf{Q} \cdot (\mathbf{r}_m - \mathbf{r}_n)}$$

The position \mathbf{r}_n is the sum of the thermal displacement and the lattice vector, $\mathbf{r}_n = \mathbf{u}_n + \mathbf{R}_n$. The instantaneous intensity can therefore be written as:

$$I(\mathbf{Q}) = |f(\mathbf{Q})|^2 \sum_{m,n} e^{i\mathbf{Q} \cdot (\mathbf{R}_m - \mathbf{R}_n)} e^{i\mathbf{Q} \cdot (\mathbf{u}_m - \mathbf{u}_n)}$$

The time averaged intensity is given by

$$\langle I(\mathbf{Q}) \rangle_{time} = |f(\mathbf{Q})|^2 \sum_{m,n} e^{i\mathbf{Q} \cdot (\mathbf{R}_m - \mathbf{R}_n)} \langle e^{i\mathbf{Q} \cdot (\mathbf{u}_m - \mathbf{u}_n)} \rangle.$$

Using the relation $\langle e^{ix} \rangle = e^{-\frac{\langle x^2 \rangle}{2}}$ gives:

$$\langle I(\mathbf{Q}) \rangle = |f(\mathbf{Q})|^2 \sum_{m,n} e^{i\mathbf{Q} \cdot (\mathbf{R}_m - \mathbf{R}_n)} e^{-\frac{\langle P_{m,n}^2 \rangle}{2}},$$

where $P_{m,n} \equiv \mathbf{Q} \cdot (\mathbf{u}_m - \mathbf{u}_n)$. The most general expression for atomic displacements in a system with extended and confined dimensions takes the form:

$$\mathbf{u}_n(t) = \sum_{\mathbf{g}, j} \mathbf{u}_{j,n}^0 \cos(\omega_j t - 2\pi \mathbf{g} \cdot \mathbf{R}_n - \delta_j),$$

where \mathbf{g} is the wavevector of the displacement wave in the extended direction, δ_j is an arbitrary phase factor, and ω_j is the angular frequency of the wave. Here $\mathbf{u}_{j,n}^0$ is a position dependent vector that captures thermal amplitudes and polarizations of phonons in the j^{th} branch of the dispersion. For instance, Bannov *et al.* use a similar expression

$$\mathbf{u}(\mathbf{R}, t) = \int \sum_j \mathbf{u}_j(\mathbf{q}, z) e^{(i\mathbf{q} \parallel \cdot \mathbf{R} \parallel - i\omega_j t)} d\mathbf{q}$$

for displacements in a GaAs/AlAs quantum well.³⁰ Returning to the general case, we have:

$$\begin{aligned} \langle P_{m,n}^2 \rangle = \sum_{\mathbf{g}, j} [& \langle \{ \mathbf{Q} \cdot \mathbf{u}_{j,m}^0 \cos(\omega_j t - 2\pi \mathbf{g} \cdot \mathbf{R}_m - \delta_j) \}^2 \rangle + \langle \{ \mathbf{Q} \cdot \mathbf{u}_{j,n}^0 \cos(\omega_j t - 2\pi \mathbf{g} \cdot \mathbf{R}_n - \delta_j) \}^2 \rangle \\ & - \langle 2(\mathbf{Q} \cdot \mathbf{u}_{j,m}^0)(\mathbf{Q} \cdot \mathbf{u}_{j,n}^0) \cos(\omega_j t - 2\pi \mathbf{g} \cdot \mathbf{R}_m - \delta_j) \cos(\omega_j t - 2\pi \mathbf{g} \cdot \mathbf{R}_n - \delta_j) \rangle] \end{aligned}$$

but $\mathbf{Q} \cdot \mathbf{u}_{j,n}^0$ is time-independent, and $\langle \{ \cos(\omega_j t - 2\pi \mathbf{g} \cdot \mathbf{R}_n - \delta_j) \}^2 \rangle = \frac{1}{2}$. This gives:

$$\begin{aligned} \langle P_{m,n}^2 \rangle = \sum_{\mathbf{g}, j} [& 1/2 \{ \mathbf{Q} \cdot \mathbf{u}_{j,m}^0 \}^2 + 1/2 \{ \mathbf{Q} \cdot \mathbf{u}_{j,n}^0 \}^2 \\ & - 2(\mathbf{Q} \cdot \mathbf{u}_{j,m}^0)(\mathbf{Q} \cdot \mathbf{u}_{j,n}^0) \langle \cos(\omega_j t - 2\pi \mathbf{g} \cdot \mathbf{R}_m - \delta_j) \cos(\omega_j t - 2\pi \mathbf{g} \cdot \mathbf{R}_n - \delta_j) \rangle] \end{aligned}$$

Using the identity $2\cos A \cos B = \cos(A+B) + \cos(A-B)$ in the expression above,

$$\langle P_{m,n}^2 \rangle = \sum_{\mathbf{g}, j} [1/2 \{ \mathbf{Q} \cdot \mathbf{u}_{j,m}^0 \}^2 + 1/2 \{ \mathbf{Q} \cdot \mathbf{u}_{j,n}^0 \}^2 - (\mathbf{Q} \cdot \mathbf{u}_{j,m}^0)(\mathbf{Q} \cdot \mathbf{u}_{j,n}^0) \cos(2\pi \mathbf{g} \cdot (\mathbf{R}_n - \mathbf{R}_m))],$$

since $\langle \cos(2\omega_j t - 2\pi \mathbf{g} \cdot (\mathbf{R}_n + \mathbf{R}_m)) \rangle = 0$, and $\cos(2\pi \mathbf{g} \cdot (\mathbf{R}_n - \mathbf{R}_m))$ is time-independent.

Let $L_m = \mathbf{Q} \cdot \mathbf{u}_{j,m}^0$ and $L_n = \mathbf{Q} \cdot \mathbf{u}_{j,n}^0$. Substituting the above expression for $\langle P_{m,n}^2 \rangle$ into the scattered intensity gives:

$$\begin{aligned} \langle I(\mathbf{Q}) \rangle &= |f(\mathbf{Q})|^2 \sum_{m,n} e^{i\mathbf{Q} \cdot (\mathbf{R}_m - \mathbf{R}_n)} e^{-\frac{\langle P_{m,n}^2 \rangle}{2}} \\ &= |f(\mathbf{Q})|^2 \sum_{m,n} e^{i\mathbf{Q} \cdot (\mathbf{R}_m - \mathbf{R}_n)} e^{-1/2 \sum_{\mathbf{g}, j} \frac{L_m^2}{2} + \frac{L_n^2}{2} - L_m L_n \cos(2\pi \mathbf{g} \cdot (\mathbf{R}_n - \mathbf{R}_m))} \\ &= |f(\mathbf{Q})|^2 \sum_{m,n} e^{i\mathbf{Q} \cdot (\mathbf{R}_m - \mathbf{R}_n)} e^{-\sum_{\mathbf{g}, j} \frac{L_m^2}{4}} e^{-\sum_{\mathbf{g}, j} \frac{L_n^2}{4}} e^{1/2 \sum_{\mathbf{g}, j} L_m L_n \cos(2\pi \mathbf{g} \cdot (\mathbf{R}_n - \mathbf{R}_m))} \end{aligned}$$

Taylor expanding the final exponential gives:

$$\begin{aligned}\langle I(\mathbf{Q}) \rangle &= |f(\mathbf{Q})|^2 \sum_{m,n} e^{i\mathbf{Q} \cdot (\mathbf{R}_m - \mathbf{R}_n)} e^{-M_m} e^{-M_n} \left[1 + \frac{1}{2} \sum_{\mathbf{g},j} L_m L_n \cos(2\pi \mathbf{g} \cdot (\mathbf{R}_n - \mathbf{R}_m)) + \dots \right] \\ &= I_0(\mathbf{Q}) + I_1(\mathbf{Q}) + \dots\end{aligned}$$

where $e^{-M_n} \equiv e^{-\Sigma_{\mathbf{g},j} \frac{L_n^2}{4}}$ serves as an “atomic Debye-Waller factor” which is now position dependent. In the limiting case where the coefficient $\mathbf{u}_{j,n}^0$ in the displacement field is spatially uniform, the sum over this pair of terms approaches the bulk Debye-Waller factor. In the above expression, $I_0(\mathbf{Q})$ is the Bragg term, and $I_1(\mathbf{Q})$ is the first-order TDS term for a finite crystal, and are given by:

$$\begin{aligned}I_0(\mathbf{Q}) &= |f(\mathbf{Q})|^2 \sum_{m,n} e^{-M_m} e^{-M_n} e^{i\mathbf{Q} \cdot (\mathbf{R}_m - \mathbf{R}_n)}, \text{ and} \\ I_1(\mathbf{Q}) &= |f(\mathbf{Q})|^2 \sum_{m,n} e^{-M_m} e^{-M_n} e^{i\mathbf{Q} \cdot (\mathbf{R}_m - \mathbf{R}_n)} \sum_{\mathbf{g},j} L_m L_n \cos(2\pi \mathbf{g} \cdot (\mathbf{R}_n - \mathbf{R}_m))\end{aligned}$$

Each of these terms can be evaluated numerically, if the displacements $\mathbf{u}_{j,n}^0$ are known. This extension of the TDS theory will be published in Fall 2013.

References

- ¹ D.G. Cahill, W.K. Ford, K.E. Goodson, G.D. Mahan, A. Majumdar, H.J. Maris, R. Merlin, and S.R. Phillpot, J. Appl. Phys. **93**, 793 (2003).
- ² A. Balandin and K.L. Wang, J. Appl. Phys. **84**, 6149 (1998).
- ³ A. Balandin and K.L. Wang, Phys. Rev. B **58**, 1544 (1998).
- ⁴ W. Liu and M. Asheghi, J. Heat Transf. **128**, 75 (2006).
- ⁵ Y.S. Ju and K.E. Goodson, Appl. Phys. Lett. **74**, 3005 (1999).
- ⁶ C. Jacoboni and L. Reggiani, Rev. Mod. Phys. **55**, 645 (1983).
- ⁷ E. Pop, R.W. Dutton, and K.E. Goodson, J. Appl. Phys. **96**, 4998 (2004).
- ⁸ M.J. Gilbert, R. Akis, and D.K. Ferry, J. Appl. Phys. **98**, 094303 (2005).
- ⁹ H. Reichert, F. Bencivenga, B. Wehinger, M. Krisch, F. Sette, and H. Dosch, Phys. Rev. Lett. **98**, 096104 (2007).
- ¹⁰ R.L. Dennis and M.B. Webb, J. Vac. Sci. Technol. **10**, 192 (1973).
- ¹¹ J. Cuffe, E. Chávez, A. Shchepetov, P.-O. Chapuis, E.H. El Boudouti, F. Alzina, T. Kehoe, J. Gomis-Bresco, D. Dudek, Y. Pennec, B. Djafari-Rouhani, M. Prunnila, J. Ahopelto, and C.M. Sotomayor Torres, Nano Lett. **12**, 3569 (2012).
- ¹² K.W. Adu, Q. Xiong, H.R. Gutierrez, G. Chen, and P.C. Eklund, Appl. Phys. Mater. Sci. Process. **85**, 287 (2006).
- ¹³ J. Qi, J.M. White, A.M. Belcher, and Y. Masumoto, Chem. Phys. Lett. **372**, 763 (2003).
- ¹⁴ K.W. Adu, H.R. Gutiérrez, U.J. Kim, G.U. Sumanasekera, and P.C. Eklund, Nano Lett. **5**, 409 (2005).
- ¹⁵ N.W. Ashcroft, *Solid State Physics* (Saunders College Publishing, 1976).
- ¹⁶ M.-M. Blum, A. Koglin, H. Ruterjans, B. Schoenborn, P. Langan, and J.C.-H. Chen, Acta Crystallograph. Sect. F Struct. Biol. Cryst. Commun. **63**, 42 (2006).
- ¹⁷ G. Gopalakrishnan, M.V. Holt, K.M. McElhinny, J.W. Spalenka, D.A. Czaplewski, T.U. Schüllli, and P.G. Evans, Phys. Rev. Lett. **110**, 205503 (2013).
- ¹⁸ C. Flensburg and R.F. Stewart, Phys. Rev. B **60**, 284 (1999).
- ¹⁹ S. Wei and M.Y. Chou, Phys. Rev. B **50**, 2221 (1994).
- ²⁰ M.A. Strosio and M. Dutta, *Phonons in Nanostructures* (Cambridge University Press, 2001).
- ²¹ A.A. Balandin, J. Nanosci. Nanotechnol. **5**, 1015 (2005).
- ²² J. Zou and A. Balandin, J. Appl. Phys. **89**, 2932 (2001).

- ²³ H. Benisty, C.M. Sotomayor-Torrès, and C. Weisbuch, *Phys. Rev. B* **44**, 10945 (1991).
- ²⁴ S.N. Klimin, E.P. Pokatilov, and V.M. Fomin, *Phys. Status Solidi B* **190**, 441 (1995).
- ²⁵ E.P. Pokatilov, D.L. Nika, V.M. Fomin, and J.T. Devreese, *Phys. Rev. B* **77**, 125328 (2008).
- ²⁶ J. Groenen, F. Poinsothe, A. Zwick, C.M. Sotomayor Torres, M. Prunnila, and J. Ahopelto, *Phys. Rev. B* **77**, 045420 (2008).
- ²⁷ C.M.S. Torres, A. Zwick, F. Poinsothe, J. Groenen, M. Prunnila, J. Ahopelto, A. Mlayah, and V. Paillard, *Phys. Status Solidi C* **1**, 2609 (2004).
- ²⁸ B.E. Warren, *X-Ray Diffraction* (Dover, 1990).
- ²⁹ H. Lamb, *Proc. R. Soc. Lond. Ser.* **93**, 114 (1917).
- ³⁰ N. Bannov, V. Aristov, V. Mitin, and M.A. Strosio, *Phys. Rev. B* **51**, 9930 (1995).
- ³¹ J.A. Rogers, M.G. Lagally, and R.G. Nuzzo, *Nature* **477**, 45 (2011).
- ³² E. Iwase, P.-C. Hui, D. Woolf, A.W. Rodriguez, S.G. Johnson, F. Capasso, and M. Lončar, *J. Micromechanics Microengineering* **22**, 065028 (2012).
- ³³ J.. Graff and E.. Schubert, *Sensors Actuators Phys.* **84**, 276 (2000).
- ³⁴ Z.Y. Dang, M. Motapothula, Y.S. Ow, T. Venkatesan, M.B.H. Breese, M.A. Rana, and A. Osman, *Appl. Phys. Lett.* **99**, (2011).
- ³⁵ K.C. Lee, *J. Electrochem. Soc.* **137**, 2556 (1990).
- ³⁶ G. Gopalakrishnan, D.A. Czaplewski, K.M. McElhinny, M.V. Holt, J.C. Silva-Martínez, and P.G. Evans, *Appl. Phys. Lett.* **102**, 033113 (2013).
- ³⁷ R. Iosub, C. Moldovan, and M. Modreanu, *Sensors Actuators Phys.* **99**, 104 (2002).
- ³⁸ M. Ahn, R.K. Heilmann, and M.L. Schattenburg, *J. Vac. Sci. Technol. B* **25**, 2593 (2007).
- ³⁹ S. Juodkazis, Y. Nishi, H. Misawa, V. Mizeikis, O. Schecker, R. Waitz, P. Leiderer, and E. Scheer, *Opt. Express* **17**, (2009).
- ⁴⁰ S.H. Lee, D.H. Kim, H.D. Yang, S.J. Kim, D.W. Shin, S.H. Woo, H.J. Lee, H.M. Seung, S.K. Lee, G.S. Lee, and J.G. Park, *J. Korean Phys. Soc.* **53**, 579 (2008).
- ⁴¹ S.. Utteridge, V.. Sashin, S.. Canney, M.. Ford, Z. Fang, D.. Oliver, M. Vos, and E. Weigold, *Appl. Surf. Sci.* **162–163**, 359 (2000).
- ⁴² C. Constancias, B. Dalzotto, P. Michallon, J. Wallace, and M. Saib, *J. Vac. Sci. Technol. B* **28**, 194 (2010).
- ⁴³ C.C. Striemer, T.R. Gaborski, J.L. McGrath, and P.M. Fauchet, *Nature* **445**, 749 (2007).
- ⁴⁴ W.M. Vanhuffelen, M.J. Deboer, and T.M. Klapwijk, *Appl. Phys. Lett.* **58**, 2438 (1991).

- ⁴⁵ V. Ziebart, O. Paul, and H. Baltes, *J. Microelectromechanical Syst.* **8**, 423 (1999).
- ⁴⁶ S. Seo, C. Euaruksakul, D.E. Savage, M.G. Lagally, and P.G. Evans, *Phys. Rev. B* **81**, 041302 (2010).
- ⁴⁷ Q.-Y. Tong, R. Gafiteanu, and U. Gösele, *Jpn. J. Appl. Phys.* **31**, 3483 (1992).
- ⁴⁸ T. Thonhauser and G.D. Mahan, *Phys. Rev. B* **69**, 075213 (2004).
- ⁴⁹ F. Murphy-Armando, G. Fagas, and J.C. Greer, *Nano Lett.* **10**, 869 (2010).